

Detection of a Pair Density Wave State in UTe₂

Qiangqiang Gu^{1§}, Joseph P. Carroll^{1,2§}, Shuqiu Wang^{3§},
Sheng Ran⁴, Christopher Broyles⁴, Hasan Siddiquee⁴,
Nicholas P. Butch⁵, Shanta R. Saha⁵, Johnpierre Paglione^{5,6},
J. C. Séamus Davis^{1,2,3,7} and Xiaolong Liu^{1,8}

1. *LASSP, Department of Physics, Cornell University, Ithaca, NY 14850, USA*
2. *Department of Physics, University College Cork, Cork T12 R5C, IE*
3. *Clarendon Laboratory, University of Oxford, Oxford, OX1 3PU, UK*
4. *Department of Physics, Washington University, St Louis, MO 63130, USA*
5. *Maryland Quantum Materials Center, University of Maryland, College Park, MD 20742, USA*
6. *Canadian Institute for Advanced Research, Toronto, Ontario M5G 1Z8, Canada*
7. *Max-Planck Institute for Chemical Physics of Solids, D-01187 Dresden, DE*
8. *Department of Physics, University of Notre Dame, Notre Dame, IN 46556, USA*

Although UTe₂ is a very promising candidate material to embody bulk topological superconductivity¹⁻¹¹, its superconductive order-parameter $\Delta(k)$ remains unknown¹². Many diverse forms for $\Delta(k)$ are physically possible¹² because, in uranium-based heavy fermion materials, strongly hybridized flat bands of composite fermions generate highly complex interactions¹³. Moreover, in such materials intertwined^{14,15} density waves of spin (SDW), charge (CDW) and pairs (PDW) may interpose, with the latter state exhibiting spatially modulating^{14,15} superconductive order-parameter $\Delta(r)$, electron pair density¹⁶⁻¹⁹ and pairing energy-gap^{17,20-23}. Hence, the newly discovered CDW state²⁴ in UTe₂ motivates the exciting prospect that a PDW state may exist in this material^{24,25}. To search for a PDW in UTe₂, we visualize the pairing energy-gap with μV – scale energy-resolution made possible by superconductive STM tips²⁶⁻²⁹ at subkelvin temperatures. We detect three PDWs, each with peak-peak gap modulations circa 10 μeV and at incommensurate wavevectors $P_{i=1,2,3}$ that are indistinguishable from the wavevectors $Q_{i=1,2,3}$ of the prevenient CDW²⁴. Concurrent visualization of the UTe₂ superconductive PDWs and the non-superconductive CDWs reveals that every $P_i:Q_i$ pair is registered to each other spatially, but with a relative phase $\delta\phi \approx \pi$. From these observations, and given UTe₂ as a spin-triplet superconductor¹², the PDW state detected here should be a spin-triplet pair density wave^{24,25}. While such states do exist³⁰ in superfluid ³He, for superconductors they are unprecedented.

1 Bulk Cooper-pair condensates are definitely topological when their superconductive or superfluid order-parameters exhibit odd parity $\Delta(\mathbf{k}) = -\Delta(-\mathbf{k})$ and consequently when each pair of fermions binds in a spin-triplet state. This situation is epitomized by liquid ^3He , which is the only known bulk topological Cooper-pair condensate^{31,32}. Although searches for an equivalent superconductor have not identified any bulk material with unambiguously topological $\Delta(\mathbf{k})$, attention has recently fixed upon the compound UTe_2 as a promising candidate¹⁻¹². This material is superconducting below the critical temperature $T_c = 1.65$ K and its extremely high critical magnetic field provided the first evidence for spin-triplet superconductivity^{1,2}. Retention of the Pauli paramagnetic susceptibility upon entering the superconducting phase as deduced from minimal suppression in the Knight shift³, is also used to adduce spin-triplet pairing. Temperature⁴, magnetic field^{4,5} and angular dependence⁵ of the superconductive quasiparticle thermal conductivity are all indicative of a superconducting energy gap with point nodes^{4,5,6}. In the superconductive phase, time-reversal symmetry breaking is signified by the appearance of a polar Kerr rotation⁷ although this is not yet detectable by muon spin rotation⁸. Additionally, the superconductive electronic structure when visualized at opposite mesa-edges at the UTe_2 (0-11) surface, breaks chiral symmetry⁹. Dynamically, the UTe_2 parent metal appears to contain both strong ferromagnetic and antiferromagnetic spin fluctuations^{10,11} relevant to superconductivity. Together these results are consistent with a spin-triplet and thus odd-parity, nodal, time-reversal symmetry breaking, chiral superconductor¹². Figure 1a shows a schematic of the crystal structure of this material, while Fig. 1c a schematic version of the Fermi surface in the (k_x, k_y) plane at $k_z = 0$ (Ref. 33). An exemplary order-parameter $\Delta(\mathbf{k})$ hypothesized⁵ for UTe_2 is also shown schematically in Fig. 1c; but numerous others have been proposed¹², including that of a PDW state^{24,25}. In theory this PDW, if generated by time-reversal and surface reflection symmetry breaking, is a spin-triplet pair density wave²⁵. Such a state is unknown for superconductors but has recently been discovered in topological superfluid ^3He ³⁰.

2 In general, an electron-pair density wave state is a superconductor but with a spatially modulating superconductive order-parameter^{14,15}. Absent flowing currents or magnetic fields, a conventional spin-singlet superconductor has order-parameter

$$\Delta_S(\mathbf{r}) = \Delta_0 e^{i\phi_S} \quad (1)$$

for which ϕ_S is the macroscopic quantum phase and Δ_0 the amplitude of the many-body condensate wavefunction. A unidirectional PDW modulates such an order-parameter at wavevector \mathbf{P} as

$$\Delta_P(\mathbf{r}) = \Delta_i(\mathbf{r})e^{i\mathbf{P}\cdot\mathbf{r}} + \Delta_{-i}(\mathbf{r})e^{-i\mathbf{P}\cdot\mathbf{r}} \quad (2)$$

meaning that the electron-pairing potential undulates spatially. By contrast, a unidirectional CDW modulates the charge density at wavevector \mathbf{Q} such that

$$\rho_Q(\mathbf{r}) = \rho_i(\mathbf{r})e^{i\mathbf{Q}\cdot\mathbf{r}} + \rho_{-i}^*(\mathbf{r})e^{-i\mathbf{Q}\cdot\mathbf{r}} \quad (3)$$

The simplest interactions between these three orders can be analyzed using a Ginzburg-Landau-Wilson (GLW) free energy density functional

$$\mathcal{F} = \lambda[\rho_Q\Delta_S^*\Delta_P + c. c.] \quad (4)$$

representing the lowest order coupling between superconductive and density wave states. There are two elementary possibilities: (a) if $\Delta_S(\mathbf{r})$ and $\Delta_P(\mathbf{r})$ are the predominant orders, they generate charge modulations of form $\rho_P(\mathbf{r}) \propto \Delta_S^*\Delta_P + \Delta_{-P}^*\Delta_S$ and $\rho_{2P}(\mathbf{r}) \propto \Delta_{-P}^*\Delta_P$, i.e. two induced CDWs controlled by the wavevector of the PDW; (b) if $\Delta_S(\mathbf{r})$ and $\rho_Q(\mathbf{r})$ are predominant orders, they generate modulations $\Delta_Q(\mathbf{r}) \propto \Delta_S^*\rho_Q$, i.e. a PDW induced at the wavevector of the CDW. In either case, the PDW state described by Eqn. 2 subsists.

3 To explore UTe₂ for such physics, it is first necessary to simultaneously visualize any coexisting CDW and PDW states. Recent experimental advances have demonstrated two techniques for visualizing a PDW state. In the first¹⁶⁻¹⁹, the condensed electron-pair density at location \mathbf{r} , $n(\mathbf{r})$, can be visualized by measuring the tip-sample Josephson critical-current squared $I_J^2(\mathbf{r})$ from which

$$n(\mathbf{r}) \propto I_J^2(\mathbf{r}) R_N^2(\mathbf{r}) \quad (5)$$

where R_N is the normal-state resistance of each Josephson junction at \mathbf{r} . In the second PDW visualization technique^{17,20-23}, the magnitude of the total energy gap $|\Delta(\mathbf{r})|$ in the sample is

defined as half the energy separation between the two superconductive coherence peaks in $N(E)$, which occur in tunneling conductance at energies $E_+(\mathbf{r})$ and $E_-(\mathbf{r})$ such that

$$|\Delta(\mathbf{r})| \equiv [E_+(\mathbf{r}) - E_-(\mathbf{r})]/2 \quad (6)$$

This can be visualized using either normal-insulator-superconductor (NIS) tunneling^{20,21,22}, or superconductor-insulator-superconductor (SIS) tunneling from superconductive STM tips^{17,23,29} whose gap energy is known *a priori*. Here we execute the second technique for UTe₂ studies.

4 UTe₂ crystals typically cleave to reveal the (0-11) surface²⁴, a schematic view of which (Fig. 1b) identifies the key atomic periodicities by vectors \mathbf{a}^* , \mathbf{b}^* . At temperature $T = 4.2$ K, this surface is visualized using STM and a typical topographic image $T(\mathbf{r})$ is shown in Fig. 1e, while Fig. 1d shows its power spectral density Fourier transform $T(\mathbf{q})$, with the surface reciprocal-lattice points identified by orange dashed circles. Under these circumstances, pioneering STM studies of UTe₂ by Aishwarya *et al*²⁴ have recently discovered a CDW state by visualizing the electronic density-of-states states $g(\mathbf{r}, E)$ with atomic resolution. As well as the standard maxima at the surface reciprocal-lattice points in $g(\mathbf{q}, E)$, the Fourier transform of $g(\mathbf{r}, E)$, Aishwarya *et al* detected three new maxima with incommensurate wavevectors $\mathbf{Q}_{1,2,3}$ signifying the existence of the CDW state occurring at temperatures up to at least $T = 10$ K. To emulate, we measure $g(\mathbf{r}, V)$ for $-25 \text{ mV} < V < 25 \text{ mV}$ at $T = 4.2$ K using a non-superconducting tip on the equivalent cleave surface to Ref. 24. Figure 2a shows a typical topographic image $T(\mathbf{r})$ of the (0-11) surface measured at 4.2 K, with the surface reciprocal-lattice points labeled by orange dashed circles in Fig. 2b, its Fourier transform $T(\mathbf{q})$. The simultaneous image $g(\mathbf{r}, 10 \text{ mV})$ in Fig. 2c exhibits the typical modulations in $g(\mathbf{r}, V)$ and its Fourier transform $g(\mathbf{q}, V)$ in Fig. 2d reveals the three CDW peaks²⁴ at $\mathbf{Q}_{1,2,3}$ labeled by blue dashed circles. Inverse Fourier filtration of these three maxima only, reveals the incommensurate CDW state of UTe₂. Overall, this state appears to consist predominantly of incommensurate charge density modulations at three (0-11) in-plane wavevectors $\mathbf{Q}_{1,2,3}$ that occur at temperatures up to 10 K²⁴, and with a characteristic energy scale up to at least ± 25 meV (Ref. 24 and Methods Section A).

5 Motivated by the discovery that this CDW exhibits an unexplained dependence on magnetic field and by the consequent hypothesis that a PDW may exist in this material^{24,25}, we next consider the possibility of direct PDW detection in UTe₂. The typical electron-tunneling signature of the UTe₂ superconducting energy-gap is exemplified in Fig. 3a left-panel, showing a density-of-states spectrum $N_{UTe_2}(E = eV) \propto dI/dV|_{NIS}(V)$ using a non-superconducting tip at $T = 280$ mK. Under these circumstances but for unknown reasons, all researchers find a minimal drop in the tunneling conductance at energies $|E| \leq |\Delta_{UTe_2}|$. One sees immediately from Fig. 3a left-panel how difficult it is to determine accurately even the basic value of the energy gap $|\Delta_{UTe_2}|$, and why such $dI/dV|_{NIS}$ spectra are quite inadequate for precision application of Eqn. 6. However, quasiparticle tunneling using superconductive tips is a well-known technique to greatly improve energy resolution. By using SIS tunneling with a tip exhibiting high sharp conductance peaks, one can profoundly enhance energy resolution for quasiparticles²⁶⁻²⁹; this has most recently been demonstrated in the development of electronic fluid flow visualization²⁹ microscopy, which required effective energy resolution $\delta E \approx 10 \mu\text{eV}$. Here, in Fig. 3a centre-panel we show the $dI/dV|_{SIS}$ spectrum²⁶ of a Nb tip on a Nb single crystal at $T = 280$ mK. This is not the density-of-states $N_{Nb}(E)$ of elemental Nb because the SIS current I is given by the convolution

$$I(V) \propto \int_0^{eV} N_{tip}(E) N_{sample}(E - eV) dE \quad (7)$$

Equation 7 demonstrates that using a superconductive tip with high sharp coherence peaks at $E_{\pm} = \pm|\Delta_{tip}|$ in $N_{tip}(E)$, will through convolution powerfully enhance the resolution for measuring the energy at which any local maxima occur in $N_{sample}(E)$. The extremely sharp maxima in Fig. 3a centre-panel then occur at energies $\pm(|\Delta_{tip}| + |\Delta_{sample}|)$ and these energies can be identified with energy resolution significantly better than $\delta E \leq 10 \mu\text{eV}$ when $T < 300$ mK²⁹. Our objective is thus to use such enhanced energy resolution techniques to visualize the energy-gap $|\Delta(\mathbf{r})|$ of UTe₂.

6 The UTe₂ samples are next cooled to $T = 280$ mK, with a consequent $T(\mathbf{r}, V)$ of the (0-11) cleave surface measured with a Nb-tip shown in Fig. 3b. Figure 3a right-panel shows a typical $dI/dV|_{SIS}$ spectrum measured on this surface using the Nb-tip at junction resistance of $R \approx 1 \text{ M}\Omega$. Here we see a powerful enhancement in the amplitude and sharpness of

maxima in $dI/dV|_{SIS}$ relative to Fig. 3a left-panel. Consequently, to determine the spatial arrangements of the energy of the two maxima $E_+(\mathbf{r}), E_-(\mathbf{r})$ exemplified in Fig. 3a right-panel, we make two separate $g(\mathbf{r}, V)$ maps in the sample-bias-voltage V ranges $-1.67 \text{ mV} < V < -1.47 \text{ mV}$ and $1.5 \text{ mV} < V < 1.7 \text{ mV}$, and in the identical field of view (FOV). The sharp peak of each $dI/dV|_{SIS}$ is fit to a second-order polynomial $dI/dV|_{SIS} = aV^2 + bV + c$, achieving typical quality of fit $R^2 = 0.98 \pm 0.04$. The energy of maximum intensity in $E_+(\mathbf{r})$ or $E_-(\mathbf{r})$ is then identified analytically from the fit parameters (Methods Section C). The fine line across Fig. 3b specifies the trajectory of an exemplary series of $dI/dV|_{SIS}$ spectra, while Fig. 3c presents the waterfall $dI/dV|_{SIS}$ spectra for both positive and negative energy coherence peaks along this line. Periodic variations in the energies at which pairs of peaks occur are obvious, directly demonstrating that $E_+(\mathbf{r})$ and $E_-(\mathbf{r})$ are modulating periodically but in energetically opposite directions. Using this $g(\mathbf{r}, V)$ measurement and fitting procedure throughout the whole FOV yields atomically resolved images of $E_+(\mathbf{r})$ and $E_-(\mathbf{r})$. The magnitude of both positive and negative superconductive energy gaps of UTe_2 is then $\Delta_{\pm}(\mathbf{r}) \equiv |E_{\pm}(\mathbf{r})| - |\Delta_{tip}|$ where $|\Delta_{tip}|$ is constant. These two independently measured gap maps $\Delta_+(\mathbf{r}), \Delta_-(\mathbf{r})$ are spatially registered to each other at every location with 27 pm precision so that the cross-correlation coefficient between them is $X \cong 0.94$. The subtending energy gap modulations are thus entirely particle-hole symmetric as evidenced by comparing Figs. 3d,e (Methods Section C).

7 From these and equivalent data, the UTe_2 superconducting energy gap structure $|\Delta_{\text{UTe}_2}(\mathbf{r})| \equiv (\Delta_+(\mathbf{r}) + \Delta_-(\mathbf{r}))/2$ can now be examined precisely for its spatial variations $\delta\Delta(\mathbf{r})$ by using

$$\delta\Delta(\mathbf{r}) \equiv |\Delta_{\text{UTe}_2}(\mathbf{r})| - \langle |\Delta_{\text{UTe}_2}(\mathbf{r})| \rangle \quad (8)$$

where $\langle |\Delta_{\text{UTe}_2}(\mathbf{r})| \rangle$ is the spatial average over the whole FOV. Figure 4a shows measured $\delta\Delta(\mathbf{r})$ in identical FOV to Fig. 3b. The Fourier transform of $\delta\Delta(\mathbf{r}), \delta\Delta(\mathbf{q})$, is presented in Fig. 4b in which the surface reciprocal-lattice points are identified by orange dashed circles. Most significantly, three additional peaks labeled by red dashed circles are observed in the energy gap modulations with incommensurate wavevectors at $\mathbf{P}_{1,2,3}$, thus representing discovery of the PDW state in UTe_2 . Focusing only on these three wavevectors $\mathbf{P}_{1,2,3}$ we perform an

inverse Fourier transform to reveal the spatial structure of the UTe₂ PDW state in Fig. 4c (Methods Section C). This state appears to consist predominantly of incommensurate superconductive energy gap modulations at three (0-11) in-plane wavevectors $\mathbf{P}_{1,2,3}$ with a characteristic energy scale 10 μeV for peak-peak modulations.

8 Given the measured energy scales and wavevectors for the CDW, SC and PDW orders (Figs. 2,4) one may now consider the two cases of intertwining outlined earlier: (a) $\Delta_S(\mathbf{r})$ and $\Delta_P(\mathbf{r})$ are predominant and generate charge modulations $\rho_P(\mathbf{r}) \propto \Delta_S^* \Delta_P + \Delta_{-P}^* \Delta_S$ and $\rho_{2P}(\mathbf{r}) \propto \Delta_{-P}^* \Delta_P$ or, (b) $\Delta_S(\mathbf{r})$ and $\rho_Q(\mathbf{r})$ are predominant and generate pair density modulations $\Delta_Q(\mathbf{r}) \propto \Delta_S^* \rho_Q$. For case (a) to be correct, a PDW with magnitude 10 μeV coexisting with a superconductor of gap maximum near 250 μeV must generate a CDW on the energy scale 25 meV and existing up to at least $T = 10$ K. For case (b) to be valid, a normal-state CDW with eigenstates at energies up to 25 meV coexisting with a superconductor of gap magnitude 250 μeV must generate a PDW at the same wavevector and with amplitude near 10 μeV . To explore this issue further, we visualize the CDW in the non-superconductive state at $T = 4.2$ K, then cool to $T = 280$ mK and visualize the PDW in precisely the same FOV. Figures 4c,d shows the result of such an experiment in the FOV of Fig. 3b. The CDW and PDW images are registered to the underlying lattice and to each other with 27 pm precision (Methods D). Comparing their coterminous images in Fig. 4c and Fig. 4d reveals that the CDW and PDW states of UTe₂ appear spatially quite distinct. Yet, they are actually registered to each other in space, being approximate negative images of each other (Fig. 4e), and with a measured relative phase for all three $\mathbf{P}_i:\mathbf{Q}_i$ pairs of $|\delta\phi_i| \cong \pi$, as shown in Fig. 4f (Methods Section D). One can see a typical example of this effect directly in a linecut across Figs. 4c,d along the Te chain direction, with the directly measured values shown in Fig. 4g. The direct and comprehensive knowledge of CDW and PDW characteristics and interactions presented in Fig. 4, now motivates search for a Ginzburg-Landau description capable of capturing this complex intertwined phenomenology and that reported in Ref. 24. Presumably this must be on the basis of second-rank tensor spin-triplet order parameters^{31,32} for both the homogeneous superconductive and the pair density wave states.

9 Notwithstanding these theoretical challenges, however, in this study we have demonstrated by direct atomic-scale visualization of the electron-pairing energy gap that three PDWs occur at incommensurate wavevectors $\mathbf{P}_{i=1,2,3}$ in UTe₂ (Figs. 4b,c). The wavevectors are indistinguishable from the wavevectors $\mathbf{Q}_{i=1,2,3}$ of the determinative normal-state CDW (Figs. 2d,4d). All three PDWs exhibit peak-peak gap energy modulations in the range near 10 μeV (Figs. 4c, g). When the $\mathbf{P}_{i=1,2,3}$ PDW states are visualized at 280 mK in the identical FOV as the $\mathbf{Q}_{i=1,2,3}$ CDWs visualized above the superconductive T_c , every $\mathbf{Q}_i: \mathbf{P}_i$ pair is spatially registered to each other (Figs. 4c,d), but with relative phase shift of $|\delta\phi_i| \cong \pi$ throughout (Fig. 4f). Given the robust evidence that UTe₂ is a spin-triplet superconductor¹², the PDW phenomenology detected and described herein (Fig. 4) signifies the entrée to spin-triplet pair density wave physics.

Fig.1

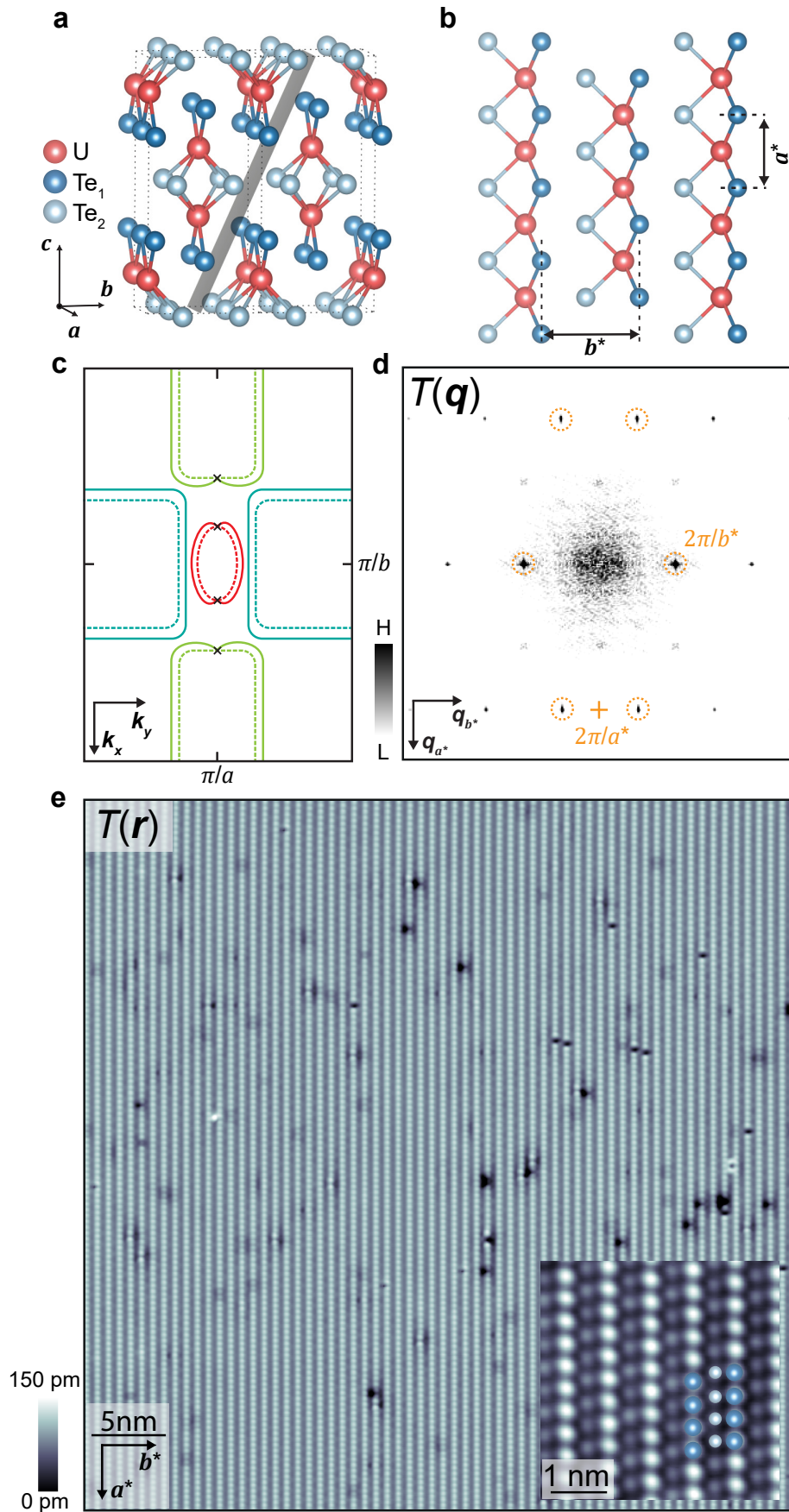


FIG. 1 Momentum-space and Real-space and Characteristics of UTe₂

- a. Schematic crystal lattice structure of UTe₂ oriented to the primary unit cell vectors **a, b, c**. The (0-11) cleave plane of UTe₂ is indicated schematically by the grey shaded plane.
- b. Schematic of elemental identities and atomic sites and unit-cell of the (0-11) termination layer of cleaved UTe₂.
- c. Schematic Fermi surface in the (k_x, k_y) plane at $k_z = 0$ for UTe₂ is indicated by dashed curves. A schematic example of one possible superconductive order parameter magnitude is indicated by solid curves representing magnitude of energy gap $\Delta(\mathbf{k})$. Here for pedagogic purposes only, is presented a chiral, spin-triplet superconductor with energy gap nodes along the **a**-axis or k_x -axis.
- d. Measured $T(\mathbf{q})$ the Fourier transform of $T(\mathbf{r})$ in $1e$, with the surface reciprocal-lattice points labeled as dashed circles. See Ref. 24.
- e. Typical topographic image $T(\mathbf{r})$ of UTe₂ (0-11) surface measured with superconducting tip at $T = 280$ mK ($I_s = 0.5$ nA, $V_s = 30$ mV). Inset: measured high resolution $T(\mathbf{r})$ at low junction resistance ($I_s = 3$ nA, $V_s = 5$ mV), clarifying two types of Te atoms.

Fig.2

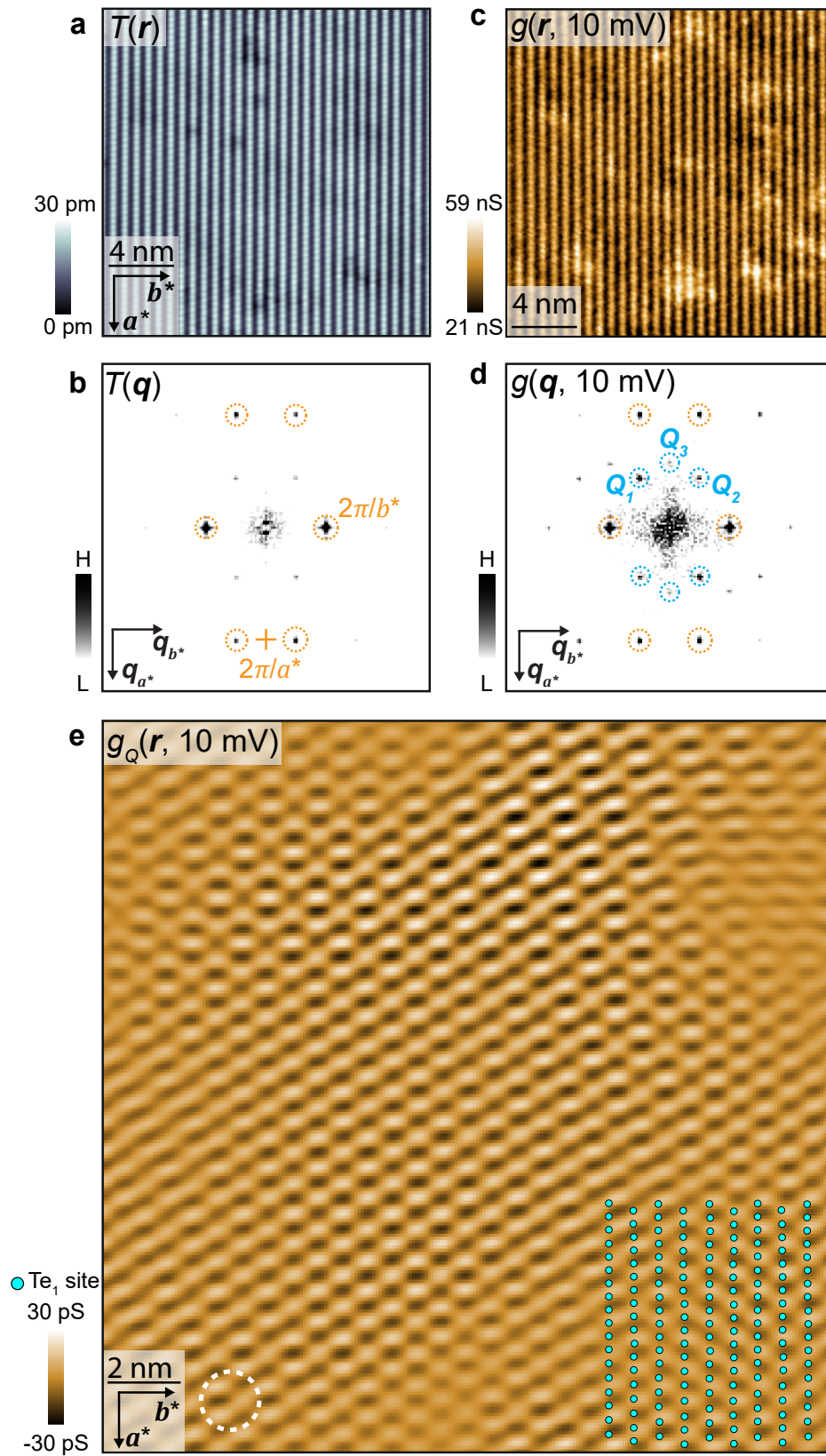


FIG 2. Visualizing the Normal-State CDW State of UTe₂

- a. Typical topographic image $T(\mathbf{r})$ of (0-11) surface measured at 4.2 K with a non-superconducting STM tip ($I_s = 1$ nA, $V_s = -30$ mV).
- b. Measured $T(\mathbf{q})$, the Fourier transform of $T(\mathbf{r})$ in 2a.
- c. Differential conductance image $g(\mathbf{r}, 10$ mV) in 2a measured at 4.2 K.
- d. Fourier transform $g(\mathbf{q}, 10$ mV) from $g(\mathbf{r}, 10$ mV) in 2c. The surface reciprocal-lattice points are labeled by orange dashed circles and the three CDW peaks at $\mathbf{Q}_{1,2,3}$ labeled by blue dashed circles.
- e. Measured density-of-states modulations $g_Q(\mathbf{r}, 10$ mV) for $E = 10$ meV only at the wavevectors $\mathbf{Q}_{1,2,3}$. This is a highly typical image of the incommensurate CDW state of UTe₂ (Methods Section A). Te₁ atomic locations of UTe₂ (0-11) surface shown as overlay.

Fig.3

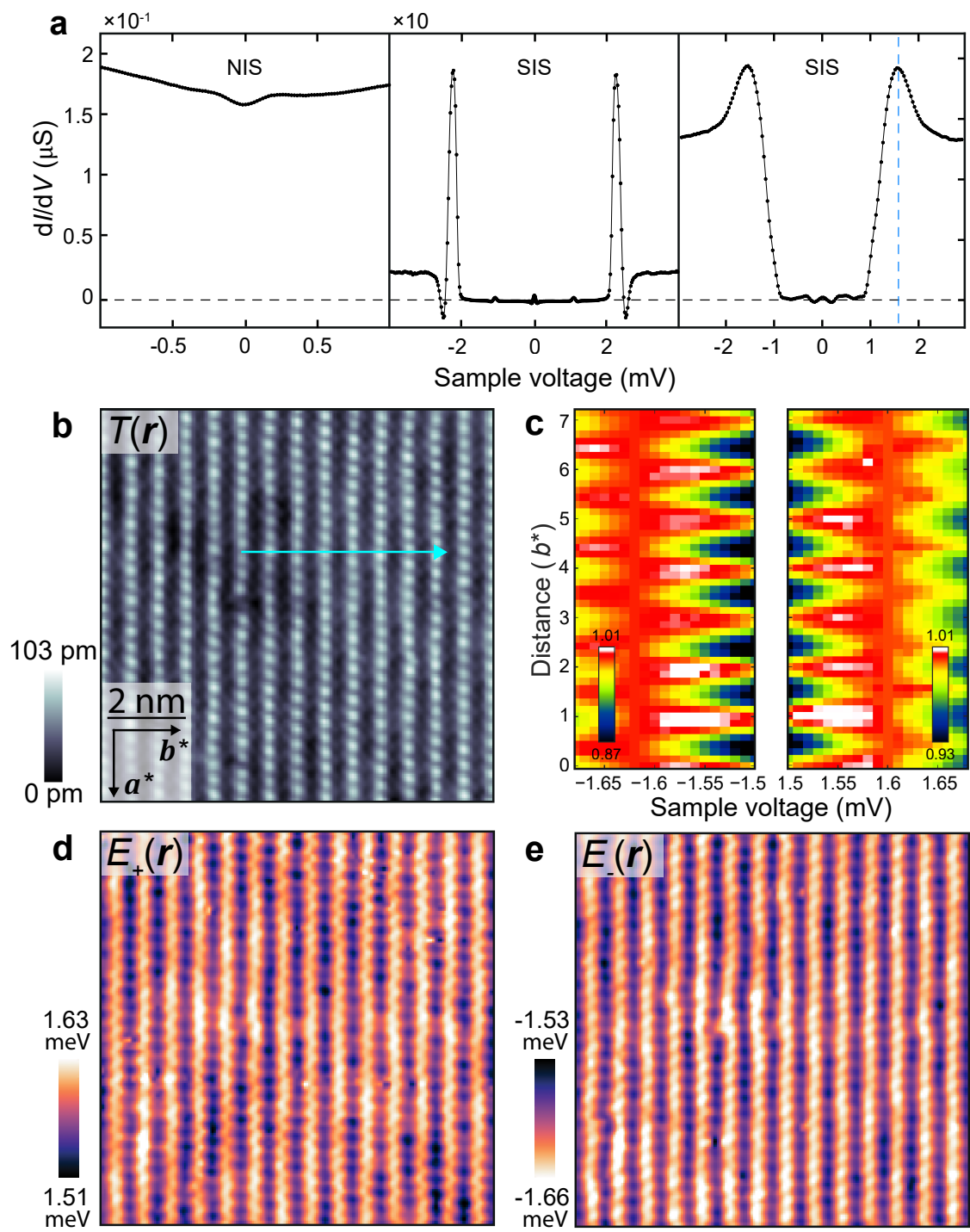


FIG. 3 Atomic-resolution Imaging the Superconductive Energy Gap of UTe₂

- a. Left: typical NIS tunneling spectrum from non-superconducting tip to UTe₂ (0-11) surface ($I_s = 1$ nA, $V_s = -5$ mV); centre: typical SIS tunneling spectrum from superconducting Nb scan tip to Nb single-crystal surface ($I_s = 8$ nA, $V_s = 4$ mV); right: typical SIS tunneling spectrum from superconducting Nb scan tip to UTe₂ (0-11) surface, a blue dashed line indicates the convoluted coherence peak of UTe₂ with Nb tip located at $|\Delta_{tip} + \Delta_{UTe_2}|$ ($I_s = 2.5$ nA, $V_s = 3$ mV). All spectra are measured at $T = 280$ mK.
- b. Typical SIS tunneling topographic image $T(\mathbf{r})$ measured at $T = 280$ mK ($I_s = 2.5$ nA, $V_s = 3$ mV). Light blue arrow shows the trajectory along which $dI/dV|_{SIS}$ spectra are presented in 3c.
- c. Exemplary $dI/dV|_{SIS}(\mathbf{r}, V)$ focused on the energy ranges near E_+ and E_- along the trajectory indicated in 3b. The modulation of the energies $E_+(\mathbf{r})$, $E_-(\mathbf{r})$ of maximum conductance are clearly seen.
- d. Measured energy $E_+(\mathbf{r})$ at which $dI/dV|_{SIS}(V_+)$ maxima occur in the same FOV as 3b. The UTe₂ empty-state superconductive energy gap is $\Delta_+(\mathbf{r}) = |E_+(\mathbf{r})| - |\Delta_{tip}|$ where $|\Delta_{tip}|$ is a constant.
- e. Measured energy $E_-(\mathbf{r})$ at which $dI/dV|_{SIS}(V_-)$ maxima occur in the same FOV as 3b. The UTe₂ filled-state superconductive energy gap is $\Delta_-(\mathbf{r}) = |E_-(\mathbf{r})| - |\Delta_{tip}|$.

Fig.4

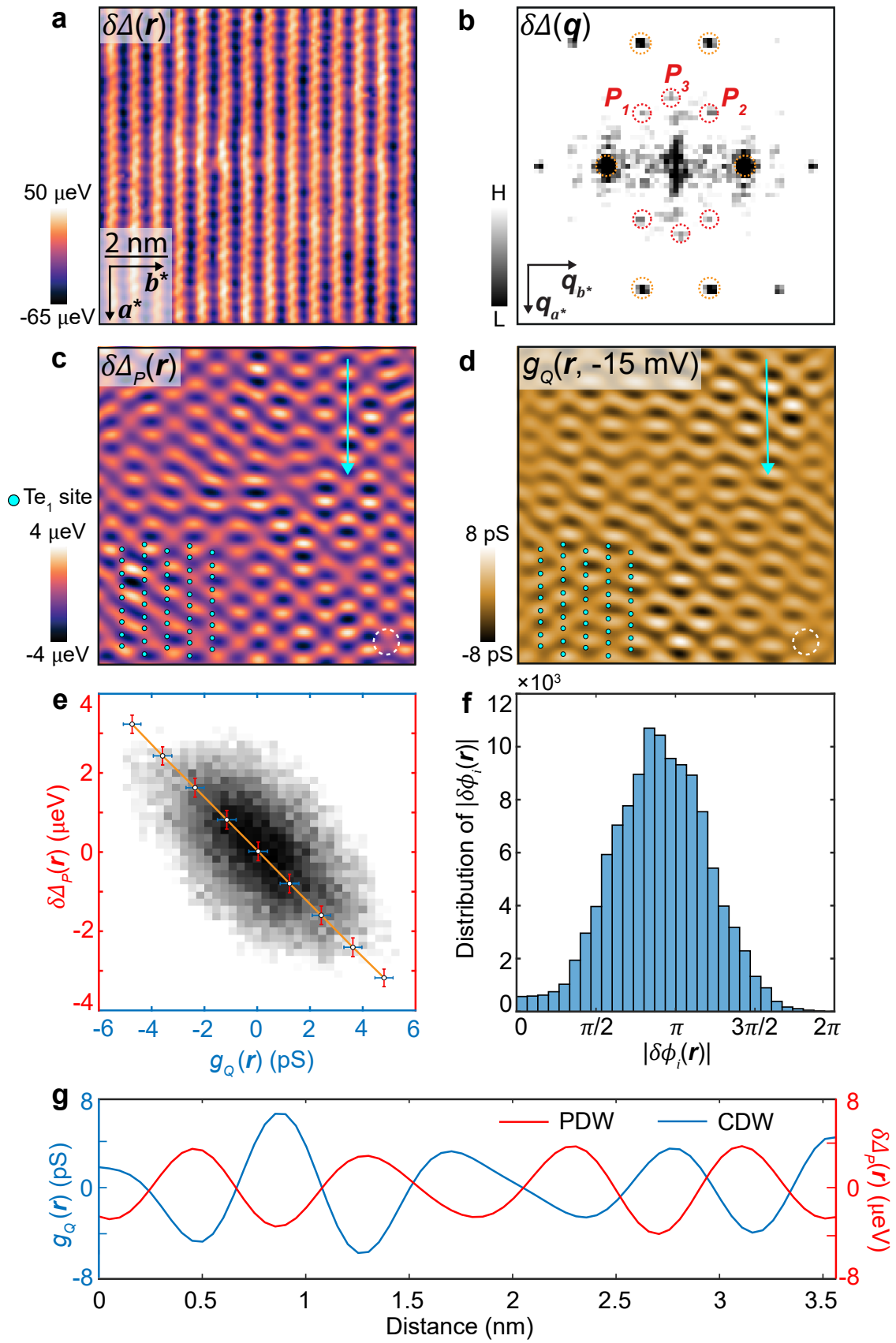


FIG. 4 Visualizing the Pair Density Wave State of UTe₂

- a. Measured variations in UTe₂ superconductive energy gap $\delta\Delta(\mathbf{r})$ in FOV of 3b.
- b. Measured $\delta\Delta(\mathbf{q})$ from 4a. The surface reciprocal-lattice points are labeled by orange dashed circles and the three PDW peaks at $\mathbf{P}_{1,2,3}$ labeled by red dashed circles.
- c. In the same FOV as 3b, inverse Fourier filtered $\delta\Delta(\mathbf{q})$ at $\mathbf{P}_{1,2,3}$ reveals the first visualization of the UTe₂ PDW state.
- d. Image of $g_Q(\mathbf{r}, -15 \text{ mV})$, i.e. of the CDW state, measured at $T = 4.2 \text{ K}$ in precisely the same FOV as 4c,3b from inverse Fourier filtered $g(\mathbf{r}, -15 \text{ mV})$ at $\mathbf{Q}_{1,2,3}$. The precision of register between every pixel in the CDW image and its equivalent in PDW image is 27 pm. These coincident CDW and PDW images are measured in the energy ranges 10 meV and 10 μeV , respectively, and appear visually quite distinct, yet their cross-correlation coefficient $X \approx -0.53$ reveals them to be anticorrelated. That is in certain areas the maxima in filled-state charge density in CDW occur at the minima of PDW energy gap.
- e. Measured statistical relationship between superconductive energy gap variations $\delta\Delta_p(\mathbf{r})$ due to PDW and charge variations $g_Q(\mathbf{r}, -15 \text{ mV})$ due to CDW for all \mathbf{r} in the FOV of 3b. The $\delta\Delta_p(\mathbf{r})$ and $g_Q(\mathbf{r}, -15 \text{ mV})$ are strongly anticorrelated spatially, meaning that $\delta\Delta_p(\mathbf{r})$ and $g_Q(\mathbf{r}, -15 \text{ mV})$ images are approximately negatives of each other.
- f. Measured statistics of the relative spatial phase difference $\delta\phi$ between the phase $\phi_i^C(\mathbf{r})$ of charge modulation at \mathbf{Q}_i and the phase $\phi_i^P(\mathbf{r})$ of energy-gap modulation at \mathbf{P}_i in the coterminous images $g_Q(\mathbf{r}, -15 \text{ mV})$ of the CDW state and $\delta\Delta_p(\mathbf{r})$ of the PDW state. Here we define $|\delta\phi_i(\mathbf{r})| \equiv |\phi_i^P(\mathbf{r}) - \phi_i^C(\mathbf{r})|$ for all pairs $\mathbf{Q}_i : \mathbf{P}_i$. The spatial phase difference between all three UTe₂ CDW and the PDW order parameters at $\mathbf{Q}_i : \mathbf{P}_i$ is thus predominantly $|\delta\phi|_{\text{RMS}} = 0.94\pi$ although there is obviously some variation about that value.
- g. Typical coterminous measurement of variations in charge density $g_Q(\mathbf{r}, -15 \text{ mV})$ and in the superconductive energy gap $\delta\Delta_p(\mathbf{r})$ along an exemplary trajectory as indicated by arrows in 4c,d.

Acknowledgements: The authors are extremely grateful to V. Madhavan for generous and incisive advice and guidance, on how to execute this project. We acknowledge and thank D. Agterberg, F. Flicker, E. Fradkin, Eun-Ah Kim, S. Simon and J. van Wezel for key discussions and theoretical guidance. Research at the University of Maryland was supported by the Department of Energy Award No. DE-SC-0019154 (sample characterization), the Gordon and Betty Moore Foundation's EPiQS Initiative through Grant No. GBMF9071 (materials synthesis), NIST, and the Maryland Quantum Materials Center. Q.G., X.L., J.P.C. and J.C.S.D. acknowledge support from the Moore Foundation's EPiQS Initiative through Grant GBMF9457. J.C.S.D. acknowledge support from the Royal Society under Award R64897. J.P.C. and J.C.S.D. acknowledge support from Science Foundation Ireland under Award SFI 17/RP/5445. S.W. and J.C.S.D. acknowledge support from the European Research Council (ERC) under Award DLV-788932.

Author Contributions: X.L. and J.C.S.D. conceived the project. S.R., C.B., H.S., S.R.S, N.P.B. and J.P. developed, synthesized and characterized materials; Q.G., J.P.C., and X.L. carried out the experiments; S.W., J.P.C. and Q.G. developed and implemented analysis. X.L. and J.C.S.D supervised the project. J.C.S.D. wrote the paper with key contributions from J.P.C., Q.G., X.L. and S.W. The paper reflects contributions and ideas of all authors.

References

- 1 Ran, S. et al. Nearly ferromagnetic spin-triplet superconductivity. *Science* **365**, 684-687 (2019).
- 2 Aoki, D. et al. Unconventional Superconductivity in Heavy Fermion UTe₂. *J. Phys. Soc. Jpn.* **88**, 043702 (2019).
- 3 Nakamine, G. et al. Superconducting Properties of Heavy Fermion UTe₂ Revealed by ¹²⁵Te-nuclear Magnetic Resonance. *J. Phys. Soc. Jpn.* **88**, 113703 (2019).
- 4 Metz, T. et al. Point-node gap structure of the spin-triplet superconductor UTe₂. *Phys. Rev. B* **100**, 220504(R) (2019).
- 5 Kittaka, S. et al. Orientation of point nodes and nonunitary triplet pairing tuned by the easy-axis magnetization in UTe₂. *Phys. Rev. Res.* **2**, 032014(R) (2020).
- 6 Xu, Y., Sheng, Y. & Yang, Y. Quasi-Two-Dimensional Fermi Surfaces and Unitary Spin-Triplet Pairing in the Heavy Fermion Superconductor UTe₂. *Phys. Rev. Lett.* **123**, 217002 (2019).
- 7 Hayes, I. et al. Multicomponent superconducting order parameter in UTe₂. *Science* **373**, 797-801 (2021).
- 8 Sundar, S. et al. Coexistence of ferromagnetic fluctuations and superconductivity in the actinide superconductor UTe₂. *Phys. Rev. B* **100**, 140502(R) (2019).
- 9 Jiao, L. et al. Chiral superconductivity in heavy-fermion metal UTe₂. *Nature* **579**, 523-527 (2020).
- 10 Tokunaga, Y. et al. ¹²⁵Te-NMR Study on a Single Crystal of Heavy Fermion Superconductor UTe₂. *J. Phys. Soc. Jpn.* **88**, 073701 (2019).
- 11 Duan, C. et al. Resonance from antiferromagnetic spin fluctuations for superconductivity in UTe₂. *Nature* **600**, 636-640 (2021).
- 12 Aoki, D. et al. Unconventional superconductivity in UTe₂. *J. Phys.: Condens. Matter* **34**, 243002 (2022).
- 13 Coleman, P. Heavy Fermions: Electrons at the Edge of Magnetism. *Handbook of Magnetism and Advanced Magnetic Materials 1*, John Wiley, Chichester, 95-148 (2007).
- 14 Fradkin, E., Kivelson, S. A. & Tranquada, J. M. Colloquium: Theory of intertwined orders in high temperature superconductors. *Rev. Mod. Phys.* **87**, 457-482 (2015).

-
- 15 Agterberg, D. F. et al. The physics of pair-density waves: cuprate superconductors and beyond. *Annu. Rev. Condens. Matter Phys.* **11**, 231–270 (2020).
 - 16 Hamidian, M. H. et al. Detection of a Cooper-pair density wave in $\text{Bi}_2\text{Sr}_2\text{CaCu}_2\text{O}_{8+x}$. *Nature* **532**, 343–347 (2016).
 - 17 Liu, X., Chong, Y. X., Sharma, R. & Davis, J. C. S. Discovery of a Cooper-pair density wave state in a transition-metal dichalcogenide. *Science* **372**, 1447–1452 (2021).
 - 18 O’Mahony, S. M. et al. On the electron pairing mechanism of Copper-Oxide high temperature superconductivity. *Proc. Natl. Acad. Sci.* **119** (37), e2207449119 (2022).
 - 19 Chen, W. et al. Identification of a nematic pair density wave state in $\text{Bi}_2\text{Sr}_2\text{CaCu}_2\text{O}_{8+x}$. *Proc. Natl. Acad. Sci.* **119** (31), e2206481119 (2022).
 - 20 Slezak, J. A. et al. Imaging the impact on cuprate superconductivity of varying the interatomic distances within individual crystal unit cells. *Proc. Natl. Acad. Sci.* **105**, 3203-3208 (2008).
 - 21 Edkins, S. D. et al. Magnetic field-induced pair density wave state in the cuprate vortex halo. *Science* **364**, 976-980 (2019).
 - 22 Choubey, P. et al. Atomic-scale electronic structure of the cuprate pair density wave state coexisting with superconductivity. *Proc. Natl. Acad. Sci.* **117**, 14805–14811 (2020).
 - 23 Du, Z. et al. Imaging the energy gap modulations of the cuprate pair-density-wave state. *Nature* **580**, 65–70 (2020).
 - 24 Aishwarya, A. et al. Magnetic-field sensitive charge density wave orders in the superconducting phase of UTe_2 . Preprint at <https://arxiv.org/abs/2207.09491> (2022).
 - 25 Yu, Y., Madhavan, V. & Raghu, S. Majorana fermion arcs and the local density of states of UTe_2 . *Phys. Rev. B* **105**, 174520 (2022).
 - 26 Pan, S. H., Hudson, E. W. & Davis, J. C. S. Vacuum tunneling of superconducting quasiparticles from atomically sharp scanning tunneling microscope tips. *Applied Physics Letters* **73**, 2992-2994 (1998).
 - 27 Randeria, M. T. et al. Scanning Josephson spectroscopy on the atomic scale. *Phys. Rev. B* **93**, 161115(R) (2016).
 - 28 Senkpiel, J. et al. Single channel Josephson effect in a high transmission atomic contact. *Comm. Phys.* **3**, 131 (2020).
 - 29 Liu, X., Chong, Y. X., Sharma, R. & Davis, J. C. S. Atomic-scale visualization of electronic fluid flow. *Nat. Mater.* **20**, 1480–1484 (2021).

-
- 30 Levitin L. V. et al. Evidence for a Spatially Modulated Superfluid Phase of ^3He under Confinement. *Phys. Rev. Lett.* **122**, 085301 (2019).
- 31 Vollhardt, D. & Wolfe, P. The Superfluid Phases of Helium 3. CRC Press (1990).
- 32 Leggett, A. J. Quantum Liquids: Bose condensation and Cooper pairing in condensed-matter systems. Oxford Graduate Texts (2006).
- 33 Miao, L. et al. Low Energy Band Structure and Symmetries of UTe_2 from Angle-Resolved Photoemission Spectroscopy. *Phys. Rev. Lett.* **124**, 076401 (2020).

Detection of a Pair Density Wave State in UTe₂

Qiangqiang Gu, Joseph P. Carroll, Shuqiu Wang, Sheng Ran, Christopher Broyles, Hasan Siddiquee, Nicholas P. Butch, Shanta R. Saha, Johnpierre Paglione, J. C. Séamus Davis and Xiaolong Liu

Materials and Methods

A Visualizing the UTe₂ CDW State

A.1 Differential Conductance Imaging of CDW at $T = 4.2$ K

At temperature $T = 4.2$ K and using the superconducting scan tip to study the UTe₂ (0-11) surface, we measure differential conductance $dI/dV(\mathbf{r}, V)$ map to visualize CDW in the normal state of UTe₂. Extended data Figs. 1a-d shows $g(\mathbf{r}, V)$ images $V = -11$ mV, -17 mV, -23 mV and -29 mV with Fourier transform $g(\mathbf{q}, V)$ shown as Extended data Figs. 1e-h. Three CDW peaks at $\mathbf{Q}_{1,2,3}$ occur in all $g(\mathbf{q}, V)$ representing incommensurate charge density modulations with a characteristic energy scale up to at least ~ 30 meV.

A.2 CDW Visualization at Incommensurate Wavevectors $\mathbf{Q}_{1,2,3}$

From these data, to calculate the amplitude $g_{Q_i}(\mathbf{r})$ of the CDW modulation represented by the peaks at \mathbf{Q}_i ($i = 1, 2, 3$), we apply a two-dimensional computational lock-in technique. Here $g(\mathbf{r})$ is multiplied by the term $e^{i\mathbf{Q}_i \cdot \mathbf{r}}$, and integrated over a Gaussian filter to obtain the lock-in signal¹

$$g_{Q_i}(\mathbf{r}) = \frac{1}{\sqrt{2\pi}\sigma_r} \int d\mathbf{R} g(\mathbf{R}) e^{i\mathbf{Q}_i \cdot \mathbf{R}} e^{-\frac{|\mathbf{r}-\mathbf{R}|^2}{2\sigma_r^2}} \quad (\text{M1})$$

where σ_r is the cut-off length in the real space. In \mathbf{q} -space this lock-in signal is

$$g_{Q_i}(\mathbf{r}) = \mathcal{F}^{-1} g_{Q_i}(\mathbf{q}) = \mathcal{F}^{-1} [\mathcal{F}(g(\mathbf{r}) e^{i\mathbf{Q}_i \cdot \mathbf{r}}) \cdot \frac{1}{\sqrt{2\pi}\sigma_Q} e^{-\frac{q^2}{2\sigma_Q^2}}] \quad (\text{M2})$$

where σ_Q is the cut-off length in \mathbf{q} -space. Here $\sigma_r = 1/\sigma_Q$. Next, $g_Q(\mathbf{r}, V)$, the inverse Fourier transform of the combined \mathbf{Q}_i ($i = 1, 2, 3$) CDWs, is then presented in Figs. 1i-l. These data demonstrate that the spatial modulations and phases of the CDW are primarily independent of energy.

To specify the filtering size of the inverse Fourier transform leading to Main Text Fig. 2e, we show in Extended Data Fig. 2 the evolution of images as a function of the real-space cut-off length σ_r . The differential conductance map $g_Q(\mathbf{r}, 10$ mV) is displayed at a series of σ_r including 10 Å, 12 Å, 14 Å, 18 Å, 24 Å and 35 Å. The distributions of the CDW domains in the filtered $g_Q(\mathbf{r}, 10$ mV) images with a cut-off length of 10 Å, 12 Å, 14 Å, 18 Å, 24 Å are highly similar. While a filter size of 35 Å leads to the vanishing of the domains. The cut-off length

used in Main Text Fig. 2e is 14 Å such that the domain of the CDW modulations are resolved, the irrelevant image distortions are excluded, and the inversed image is consistent with the results from other cut-off lengths. It resolves the CDW domain structures without picking up irrelevant contributions from other wavevectors. Same filter size of 14 Å is chosen for all three Q -vectors.

Formally the same inversed Fourier transform analysis is carried out for main text Figs. 4c-d, but with a filter size of 7.9 Å to filter CDW and PDW peaks.

A.3 Simulated UTe_2 Topography

To identify q -space peaks resulting from the (0-11) cleave plane structure of UTe_2 we simulate the topography of the UTe_2 cleave plane and Fourier transform this simulation. Subsequently we are able to distinguish clearly the CDW signal from the structural periodicity of the surface. The simulation is calculated based on the ideal lattice constant of the (0-11) plane of the UTe_2 , $a^* = 4.16$ Å and inter-Te-chain distance $b^* = 7.62$ Å. Extended Data Fig. 3a is a simulated $T(\mathbf{r})$ image in FOV of 14.5 nm. The simulated topography $T(\mathbf{r})$ is in a good agreement with experimental $T(\mathbf{r})$ images presented throughout in the paper. The Fourier transform, $T(\mathbf{q})$, of the simulated $T(\mathbf{r})$ in Extended Data Fig. 3b shows six sharp peaks, confirming that they are the primary peaks resulting from the cleave plane structure. Most importantly, the CDW peaks in Fig. 2d are not seen in the simulation. They are therefore not caused by the surface periodicity but instead originate from the electronic structure.

B UTe_2 sample and Nb tip preparation

B.1 Sample preparation

High-quality UTe_2 single crystals were synthesized by chemical vapor transport using iodine as the transport agent. The UTe_2 crystal is mounted on the sample holder such that the (0-11) cleave plane is facing upwards. The sample is cleaved in situ in a cryogenic ultrahigh vacuum environment at ~ 4.2 K, and immediately inserted into the STM head. STM measurements are performed using a custom-built STM at a base temperature of ~ 280 mK. The STM is controlled using SPECS Nanonis electronics.

B.2 Tip preparation

Atomic-resolution superconducting Nb tips are formed by field emission of a Nb wire on a Nb single-crystal target. The total gap value of superconducting tip and Nb target is determined at the energy of a sharp coherence peak (middle panel Main Text Fig. 3a). To determine the tip gap value during our experiments, we measure dI/dV spectrum on UTe_2 at 1.5 K ($T_c = 1.65$ K), where the UTe_2 superconducting gap is closed. Thus the tip gap value

$|\Delta_{tip}|$ is taken as ~ 1.37 meV from the energy of the coherence peak (black curve in Extended Data Fig. 4). When the temperature cooled down to 280 mK, the measured spectrum shows almost the same coherence peak energy (blue curve in Extended Data Fig. 4), indicating the negligible contribution of the UTe₂ gap at large junction resistances. While at a very small junction resistance of ~ 1 M Ω , SIS junction current I is given by the convolution of the density-of-states of superconducting tip and superconducting UTe₂, the typical $dI/dV|_{SIS}$ taken at 280 mK on UTe₂ (the right panel Main Text Fig. 3a) shows the total gap value $|\Delta_{tip}| + |\Delta_{UTe_2}| = 1.62$ meV. Therefore we estimate $|\Delta_{UTe_2}| \sim 0.25$ meV, being consistent with the previous report and the $dI/dV|_{NIS}$ shown as the left panel in Main Text Fig. 3a.

C Visualizing UTe₂ Electron-Pairing Energy Gap $\Delta(\mathbf{r})$

C.1 Nb Coherence-peak Amplified UTe₂ Energy Gap

To determine the energy of $E_+(\mathbf{r})$ and $E_-(\mathbf{r})$ at which the maximum conductance occurs, we fit the peak of the measured $dI/dV|_{SIS}(V)$ spectra using a second-order polynomial fit (Equation M3).

$$dI/dV|_{SIS}(V) = aV^2 + bV + c \quad (\text{M3})$$

The polynomial fits excellently with the experimental data. Extended Data Fig. 5a shows the fitting of a typical $dI/dV|_{SIS}(V)$ spectrum, and the evolution of fits $dI/dV|_{SIS}(V)$ along a representative line is shown in Extended Data Fig. 5b and it demonstrates a clear gap modulation. The fitting quality is defined using the coefficient

$$R^2(\mathbf{r}) = 1 - \frac{\sum_{i=1}^N [g(\mathbf{r}, V_i) - dI/dV|_{SIS}(\mathbf{r}, V_i)]^2}{\sum_{i=1}^N [g(\mathbf{r}, V_i) - \bar{g}(\mathbf{r})]^2}$$

The statistical histogram of the coefficient R^2 from the whole field of view can be quantitatively seen in Extended Data Fig. 5c. The mean value $\langle R^2 \rangle = 0.98 \pm 0.04$ indicates excellent fitting quality in the gap maps $\Delta_+(\mathbf{r})$ and $\Delta_-(\mathbf{r})$.

C.2 Shear correction and Lawler-Fujita algorithm

To register multiple images to precisely the same field of view, a shear correction technique and the Lawler-Fujita (LF) algorithm² are implemented to the experimental data. To recover the arbitrary hexagon of the Te lattice, shear correction is applied to correct any image distortions caused by long-range scanning drift. The coordinate system in the experimental data \mathbf{r} is transformed to a coordinate system $\tilde{\mathbf{r}}$ that has the crystal symmetry of the UTe₂ lattice. The transformation in the x -direction with magnitude p is described as

$$\begin{pmatrix} x \\ y \end{pmatrix} = \mathbf{S} \begin{pmatrix} \tilde{x} \\ \tilde{y} \end{pmatrix} \quad (\text{M4})$$

where $\mathbf{S} = \begin{bmatrix} 1 & p \\ 0 & 1 \end{bmatrix}$ is the transformation matrix. In \mathbf{q} -space, this leads to a transformation of $\tilde{Q}_y \rightarrow \tilde{Q}_y - p\tilde{Q}_x$. Consider an arbitrary triangular lattice with two adjacent Bragg peaks \tilde{Q}_1 and \tilde{Q}_2 with angles α and $\alpha + 1.295$ from the Q_x -axis, respectively. A shear at an angle θ from the Q_x -axis will transform \tilde{Q}_i into the following

$$\mathbf{Q}_1 = \begin{pmatrix} q_1 \cos \alpha + p q_1 \sin \theta \cos(\theta - \alpha) \\ q_1 \sin \alpha + p q_1 \cos \theta \cos(\theta - \alpha) \end{pmatrix} \quad (\text{M5})$$

$$\mathbf{Q}_2 = \begin{pmatrix} q_2 \cos(\alpha + 2.59) + p q_2 \sin \theta \cos(\theta - \alpha - 2.59) \\ q_2 \sin(\alpha + 2.59) + p q_2 \cos \theta \cos(\theta - \alpha - 2.59) \end{pmatrix} \quad (\text{M6})$$

Where $q_1 = |\tilde{Q}_1|$, $q_2 = 1.912 * |\tilde{Q}_1|$. p and θ are determined by solving Equation M5-6 using measured \mathbf{Q}_1 and \mathbf{Q}_2 . The angle coefficient 1.295 and the vector length coefficient 1.912 are estimated from the simulated Fourier transform of an ideal UTe_2 lattice in Extended Data Fig. 3b. Consequently the shear corrected image can be obtained by the transformation $\tilde{T}(\tilde{\mathbf{r}}) = T(\mathbf{r})$. Here the two coordinate systems \mathbf{r} and $\tilde{\mathbf{r}}$ are related by the transformation $\tilde{\mathbf{r}} = \mathbf{R}^{-1} \mathbf{S}^{-1} \mathbf{R} \mathbf{r}$, where \mathbf{R} is the rotation matrix with angle $-\theta$.

To obtain the perfectly periodic lattice, we apply the LF algorithm. Let $\tilde{T}(\tilde{\mathbf{r}})$ represent a topograph of a perfect UTe_2 lattice without any distortion. Three pairs of Bragg peaks \mathbf{Q}_1 , \mathbf{Q}_2 and \mathbf{Q}_3 can be obtained from FT of $\tilde{T}(\tilde{\mathbf{r}})$. Hence $\tilde{T}(\tilde{\mathbf{r}})$ is expected to take the form

$$\tilde{T}(\tilde{\mathbf{r}}) = \sum_{i=1}^3 T_i \cos(\mathbf{Q}_i \cdot \tilde{\mathbf{r}} + \theta_i), \quad (\text{M7})$$

The experimentally obtained topography $T(\mathbf{r})$ may suffer from a slowly varying position-dependent spatial phase shift $\theta_i(\mathbf{r})$, which can be given by

$$T(\mathbf{r}) = \sum_{i=1}^3 T_i \cos(\mathbf{Q}_i \cdot \mathbf{r} + \theta_i(\mathbf{r})), \quad (\text{M8})$$

To get $\theta_i(\mathbf{r})$, we employ a computational two-dimensional lock-in technique to the topography

$$A_{\mathbf{Q}}(\mathbf{r}) = \int d\mathbf{R} T'(\mathbf{R}) e^{i\mathbf{Q} \cdot \mathbf{R}} e^{-\frac{(\mathbf{r}-\mathbf{R})^2}{2\sigma^2}}, \quad (\text{M9})$$

$$A_{\mathbf{Q}_i}(\mathbf{r}) = \mathcal{F}^{-1} A_{\mathbf{Q}_i}(\mathbf{q}) = \mathcal{F}^{-1} [\mathcal{F}(T'(\mathbf{r}) e^{i\mathbf{Q}_i \cdot \mathbf{r}}) \cdot \frac{1}{\sqrt{2\pi}\sigma_{\mathbf{Q}}} e^{-\frac{q^2}{2\sigma_{\mathbf{Q}}^2}}], \quad (\text{M10})$$

$$|A_{\mathbf{Q}}(\mathbf{r})| = \sqrt{\left(\text{Re} A_{\mathbf{Q}}(\mathbf{r})\right)^2 + \left(\text{Im} A_{\mathbf{Q}}(\mathbf{r})\right)^2}, \quad (\text{M11})$$

$$\theta_i(\mathbf{r}) = \tan^{-1} \frac{\text{Im} A_{\mathbf{Q}_i}(\mathbf{r})}{\text{Re} A_{\mathbf{Q}_i}(\mathbf{r})}. \quad (\text{M12})$$

where σ is chosen to capture the lattice distortions. In the Lawler-Fujita analysis, we use $\sigma_q = 3.8 \text{ nm}^{-1}$. Mathematically, the relationship between the distorted and the perfect lattice for each \mathbf{Q}_i is $\mathbf{Q}_i \cdot \mathbf{r} + \theta_i(\mathbf{r}) = \mathbf{Q}_i \cdot \tilde{\mathbf{r}} + \theta_i$. We define another global position-

dependent quantity, the displacement field $\mathbf{u}(\mathbf{r}) = \mathbf{r} - \tilde{\mathbf{r}}$, which can be obtained by solving equations

$$\mathbf{u}(\mathbf{r}) = \begin{pmatrix} \mathbf{Q}_1 \\ \mathbf{Q}_2 \\ \mathbf{Q}_3 \end{pmatrix}^{-1} \begin{pmatrix} \theta_1 - \theta_1(\mathbf{r}) \\ \theta_2 - \theta_2(\mathbf{r}) \\ \theta_3 - \theta_3(\mathbf{r}) \end{pmatrix}. \quad (\text{M13})$$

Finally, a drift-corrected topography, $\tilde{T}(\tilde{\mathbf{r}})$ is obtained by

$$\tilde{T}(\tilde{\mathbf{r}}) = T(\mathbf{r} - \mathbf{u}(\mathbf{r})). \quad (\text{M14})$$

By applying the same correction of $\mathbf{u}(\mathbf{r})$ to the simultaneously taken differential conductance map $g(\mathbf{r})$, we can get

$$\tilde{g}(\tilde{\mathbf{r}}) = g(\mathbf{r} - \mathbf{u}(\mathbf{r})). \quad (\text{M15})$$

where $\tilde{g}(\tilde{\mathbf{r}})$ is the drift-corrected differential conductance map.

C.3 Lattice Registration of UTe₂ Energy Gap $\Delta(r)$

Due to the small junction resistance $\sim 1 \text{ M}\Omega$ between Nb tip and UTe₂ sample during the $dI/dV|_{\text{SIS}}(V)$ map measurement, if we take the maps at both positive and negative energy sides simultaneously, the flip of bias polarity will immediately change the direction of electric field applied in the tunneling junction, which may affect the stability of the last atom on the STM tip. Hence we make two separate $g(\mathbf{r}, V)$ maps separated by several days, and in two overlapping FOVs, with energy ranges $-1.67 \text{ meV} < E < -1.47 \text{ meV}$ and $1.5 \text{ meV} < E < 1.7 \text{ meV}$. Therefore, we obtain two datasets, $T_+(\mathbf{r})$ with the simultaneous $g_+(\mathbf{r}, V)$ at positive bias and $T_-(\mathbf{r})$ with the simultaneous $g_-(\mathbf{r}, V)$ at negative bias.

After the shear and LF correction are applied, the lattice in the corrected topographs of $T_+(\mathbf{r})$ and $T_-(\mathbf{r})$ become nearly perfectly periodic. Next, we perform rigid spatial translations to register the two topographs to the exact same FOV with a lateral precision better than 27 pm. Extended Data Figs. 6a-b shows two topographs of registered $T_+(\mathbf{r})$ and $T_-(\mathbf{r})$. Cross-correlation (XCORR) of two images I_1 and I_2 , $C(\mathbf{r}, I_1, I_2)$ at \mathbf{r} is obtained by sliding two images \mathbf{r} apart and calculate the convolution,

$$C(\mathbf{r}, I_1, I_2) = \frac{\int I_1^*(\mathbf{r}_1) I_2(\mathbf{r} + \mathbf{r}_1) d\mathbf{r}_1}{\sqrt{\int |I_1(\mathbf{r}_1)|^2 d\mathbf{r}_1 \int |I_2(\mathbf{r}_2)|^2 d\mathbf{r}_2}}. \quad (\text{M16})$$

where the denominator is a normalization factor such that when I_1 and I_2 are exactly the same image, we can get $C(\mathbf{r} = \mathbf{0}, I_1, I_2) = 1$ with the maximum centered at (0,0) cross-correlation vector. Extended Data Fig. 6c shows the maximum of XCORR between $T_+(\mathbf{r})$ and $T_-(\mathbf{r})$ coincides with the (0,0) cross-correlation vector. The offset of the two registered images are within one pixel. The uncertainty of registration is half the size of the single pixel. Thus we prove the precision of the multiple-image registration method is better than 0.5 pixel = 27 pm in the whole FOV. The maxima of the cross-correlation coefficient between the topographs is 0.95, where a coefficient of 1 indicates two identical images. All transformation

parameters applied to $T_+(\mathbf{r})$ and $T_-(\mathbf{r})$ to yield the corrected topographs are subsequently applied to the corresponding $dI/dV|_{SIS}(V)$ maps taken at positive and negative voltage.

C.4 Particle-hole Symmetry of UTe_2 Energy Gap $\Delta(\mathbf{r})$

The cross-correlation map in Extended Data Fig. 7a provides a two-dimensional measure of agreement between the positive and negative $dI/dV|_{SIS}(V)$ conductance peak maps. Extended Data Fig. 7b shows a linecut along the trajectory indicated in Extended Data Fig. 7a. It shows a maximum of 0.94 and coincides with the (0,0) cross-correlation vector. The higher value of XCORR indicates the growing similarity between the two images, and XCORR of 1 indicates two identical images. Thus it shows that gap values between positive bias and negative bias are highly correlated, demonstrating the expected particle-hole symmetry of PDW energy gap magnitudes for superconducting UTe_2 .

C.5 PDW Visualization at Incommensurate Wavevectors $P_{1,2,3}$

The inverse Fourier transform analysis for PDW state in Main Text Fig. 4c is implemented using the same technique described in Section A.2. The filter size chosen to visualize the PDW is 7.9 Å such that the domain structures are resolved and irrelevant image distortion is excluded. The inverse Fourier transform of the CDW in Main Text Fig. 4d is calculated using the identical filter size of 7.9 Å.

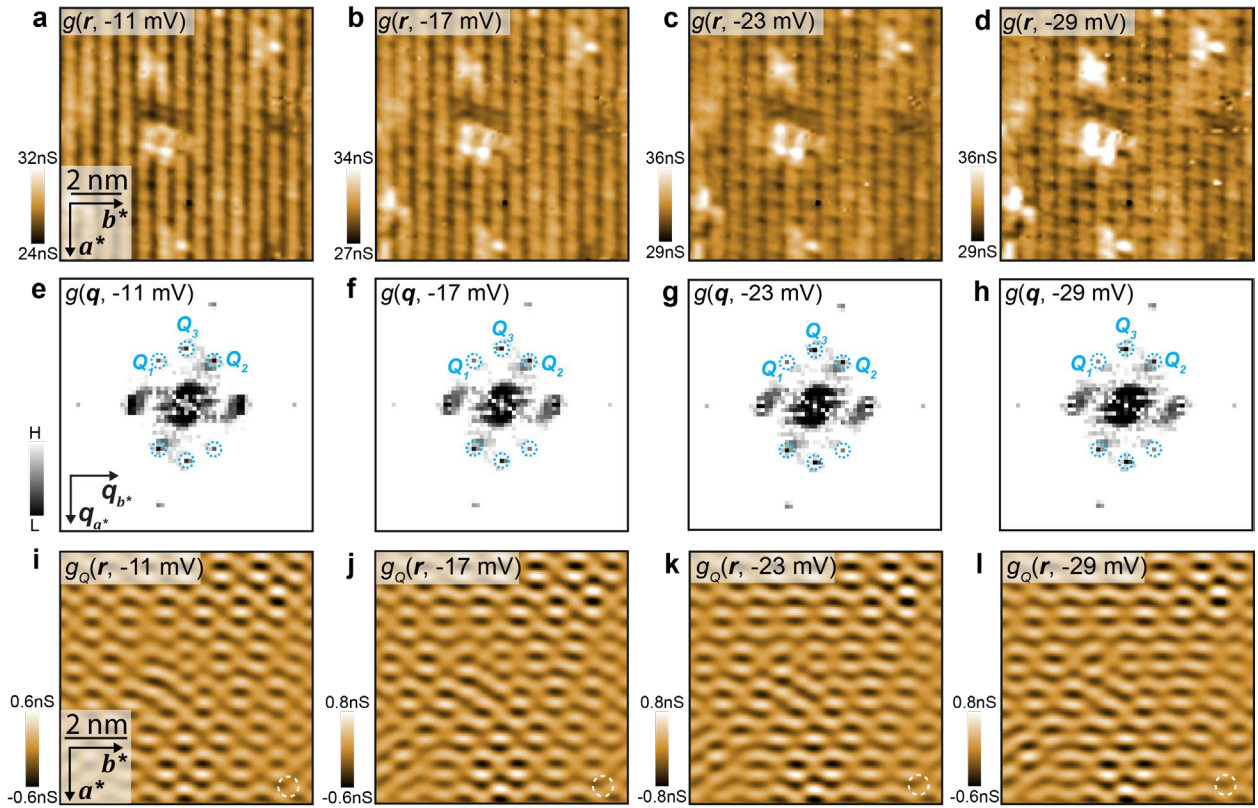
C.6 Independent PDW Visualization Experiments

To confirm that the PDW phase discovered is present in multiple FOVs we show a typical example of the gap modulation $\Delta(\mathbf{r})$ from one different field of view in Extended Data Fig. 8. The $g(\mathbf{r}, V)$ map is measured in the voltage region surrounding the positive Nb- UTe_2 coherence peak. The FOV is fitted with a second-order polynomial as in Section C.1, and shear correction and LF algorithm are implemented as in C.2. The resulting map, $\delta\Delta_+(\mathbf{r})$ is presented in Extended Data Fig. 8b. The Fourier transform of this map, $\delta\Delta_+(\mathbf{q})$ is presented in Extended Data Fig. 8c. $\delta\Delta_+(\mathbf{q})$ features the same PDW wavevectors, (P_1, P_2, P_3) observed in the main text.

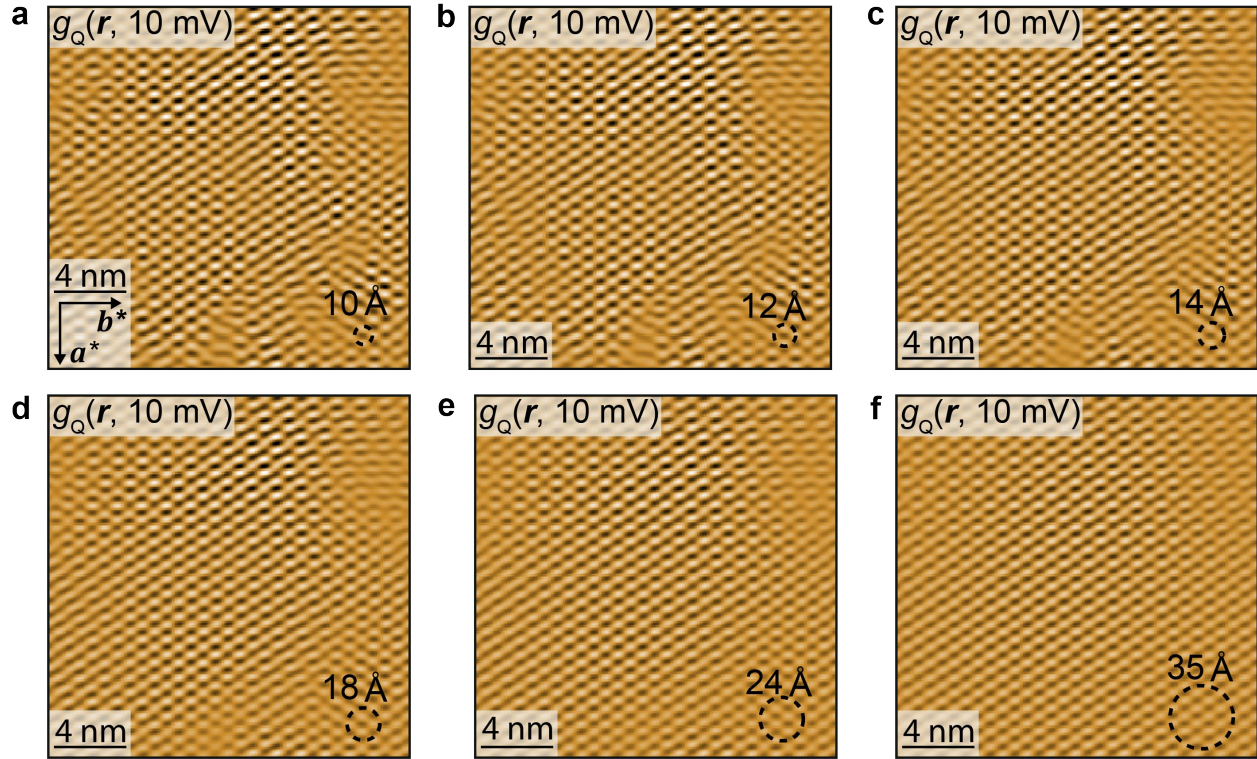
D **Relative phase shift between all CDW: PDW pairs**

The analysis of phase difference between PDW and CDW at three different Q -vectors is shown in Extended Data Fig. 9. The Inverse Fourier transforms of each CDW and PDW wavevector demonstrate a clear half-period shift between the two density waves (First and second row in Extended Data Fig. 9). This shift motivates the statistical analysis of the phase difference. The phase map of $g_{Q_1}(\mathbf{r}, -15 \text{ mV})$, $\phi_1^C(\mathbf{r})$, and the phase map of $\Delta_{P_1}(\mathbf{r})$, $\phi_1^P(\mathbf{r})$, are calculated using Equation M12. The phase difference between two corresponding maps

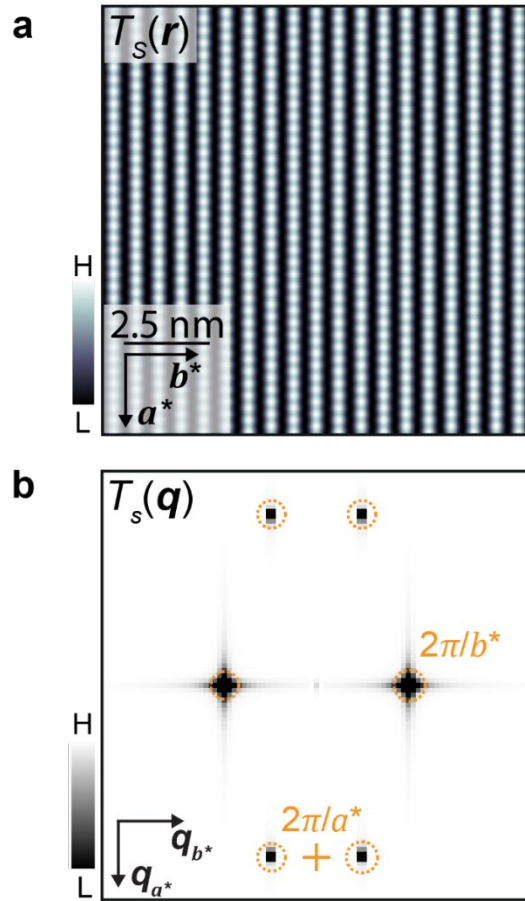
is defined as $|\delta\phi_1| = \phi_1^C(\mathbf{r}) - \phi_1^P(\mathbf{r})$ for the $\mathbf{P}_1: \mathbf{Q}_1$ wavevectors. The identical procedure is carried out for $\mathbf{P}_2: \mathbf{Q}_2$ and $\mathbf{P}_3: \mathbf{Q}_3$. The histograms resulting from this procedure show that the statistical distributions of the phase shift $|\delta\phi_i|$ are centered around π . Although the distribution varies, this π phase shift reinforces the observation of the spatial anti-correlation between CDW and PDW.



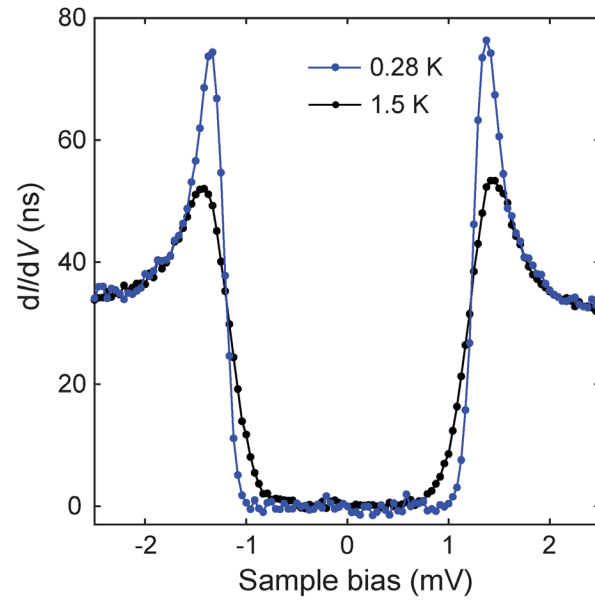
Extended Data Fig. 1 CDW at different voltages in UTe₂. **a.** Measured $g(r, V)$ images of UTe₂ using superconductive STM tips at $T = 4.2$ K, and at four representative negative sample voltages including -11 mV, -17 mV, -23 mV and -29 mV in the same $10 \text{ nm} \times 10 \text{ nm}$ field of view. **b.** Fourier transform of the $g(r, V)$ images, $g(q, V)$, showing the presence of the three wavevectors corresponding to the CDW order (labelled by dashed blue circles). **c.** Inverse Fourier transform the CDW peaks (Q_1, Q_2, Q_3) at different sample voltages. The CDW pattern is independent from the sample voltages for $-29 \text{ mV} < V < -11 \text{ mV}$. A white dashed circle indicates σ of Gaussian filter used to isolate CDW peaks in real space.



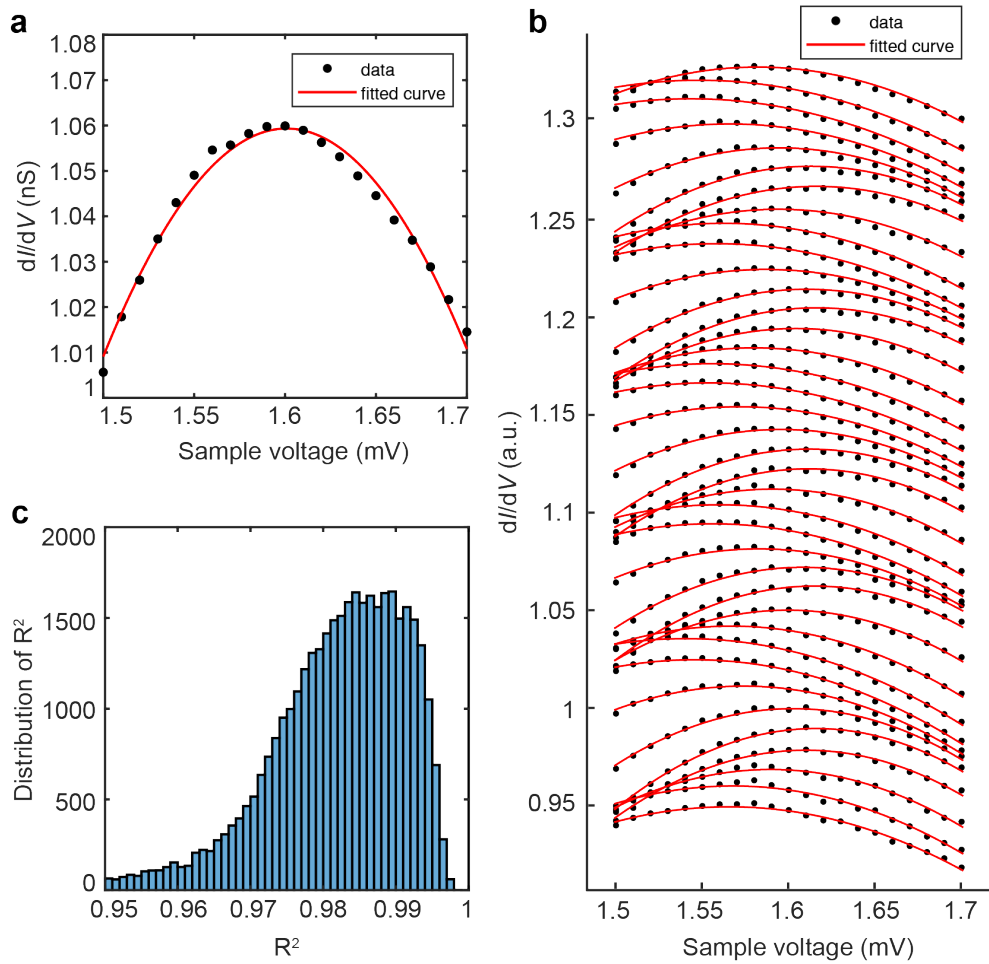
Extended Data Fig. 2 Cut-off dependence of inverse Fourier filtering $g_Q(r, 10 \text{ mV})$. Inverse Fourier transform of CDW peaks from $g_Q(r, 10 \text{ mV})$ map. The images of $g_Q(r, 10 \text{ mV})$ are filtered at different cut-off lengths such as 10 Å, 12 Å, 14 Å, 18 Å, 24 Å and 35 Å. The filter size is indicated as a dashed black circle in the bottom-right corner. Smaller values of σ_r introduce more of surrounding noise in the Fourier transform $g_Q(q, 10 \text{ mV})$ and lead to less defined domain borders. σ_r chosen for main text Fig. 2e is 14 Å.



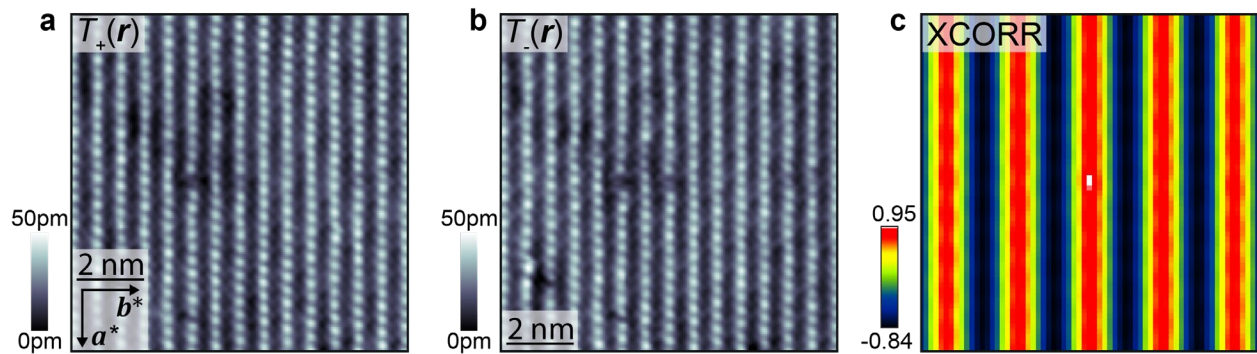
Extended Data Fig. 3 Simulated topography of UTe₂ and its Fourier transform. a. Simulated topograph, $T_s(\mathbf{r})$ of (0-11) cleave surface of UTe₂. **b.** Fourier transform of simulated topograph, $T_s(\mathbf{q})$. The six primary peaks are signal from the crystal structure of UTe₂. They are observed in the experimental STM data.



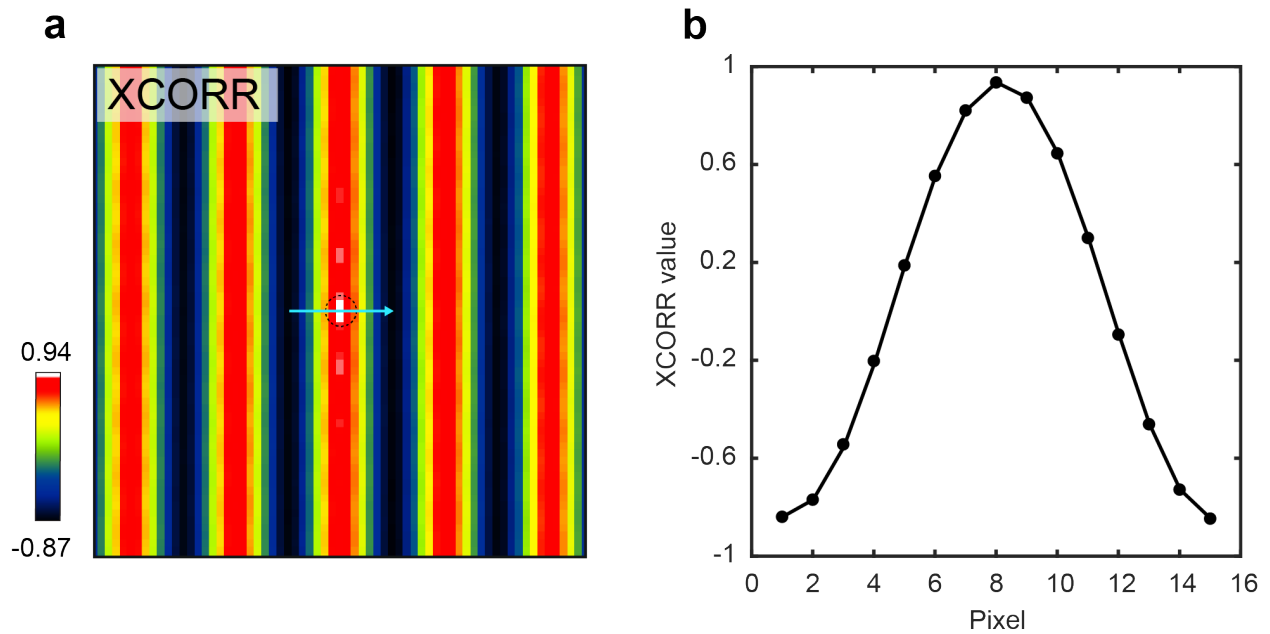
Extended Data Fig. 4 SIS tunneling spectrum measuring the tip gap Δ_{tip} . Two typical spectra measured at a large junction resistance 40 M Ω . The tip gap Δ_{tip} is found to be 1.37 meV. The coherence peak value is unaffected by temperature indicating the negligible contribution of the UTe₂ gap at large junction resistances.



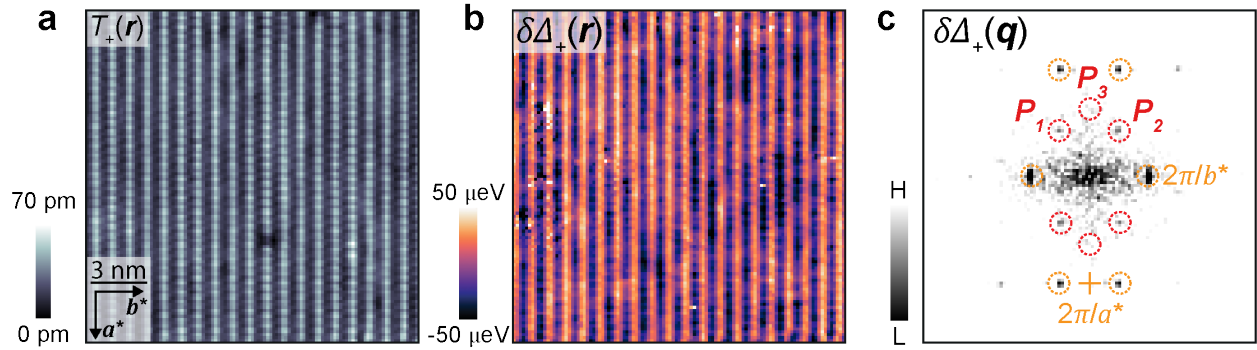
Extended Data Fig. 5 Gap determination and fitting quality. **a.** Example of polynomial fitting (red line) on dI/dV data (black points) from 1.5 mV to 1.7 mV. The peak energy value is estimated by fitting the second order polynomial $dI/dV|_{SIS} = aV^2 + bV + c$ and calculating the first derivative. **b.** An evolution of fits $dI/dV|_{SIS}(V)$ along a representative line. **c.** Histogram of the coefficient of determination R^2 . Averaged value of $\langle R^2 \rangle = 0.976 \pm 0.043$.



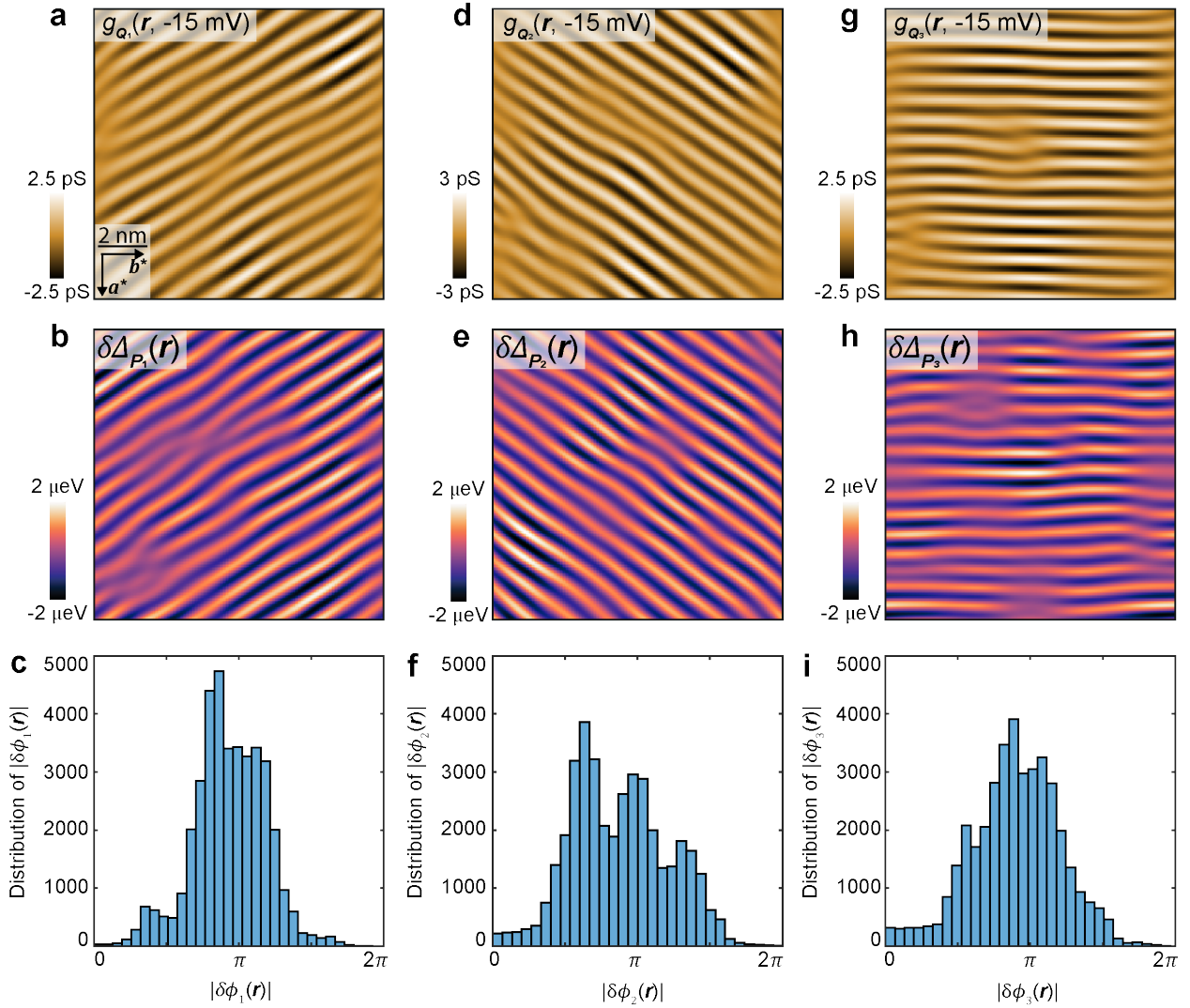
Extended Data Fig. 6 Spatial Registration of topographs. a-b 10 nm × 10 nm topographs after registration. These topographs were obtained concomitantly as dI/dV maps recording positive and negative coherence peaks respectively. **c.** Cross-correlation (XCORR) map of the registered topographs. The correlation coefficient is 0.95 indicating the two topographs are almost identical. The maxima of the XCORR map is single pixel wide, which suggests a registration precision of 0.5 pixels equivalent to real registration precision of 27 pm.



Extended Data Fig. 7 Cross-correlation of gap map $\Delta_+(\mathbf{r})$ and $\Delta_-(\mathbf{r})$. **a** Cross-correlation (XCORR) map providing a two-dimensional measure of correlation between the positive gap map $\Delta_+(\mathbf{r})$ and negative gap map $\Delta_-(\mathbf{r})$. **b** A linecut along the trajectory indicated in **a**. It shows the maximum is 0.94 and coincides with the (0,0) cross-correlation vector. The strong correlation demonstrates the particle-hole symmetry in UTe_2 .



Extended Data Fig. 8 PDW repeatability analysis. **a.** A topograph recorded in a new FOV away from that seen in Main Text Fig. 3b. The image size is $15 \text{ nm} \times 15 \text{ nm}$ ($V_s = 3 \text{ mV}$, $I_s = 2.5 \text{ nA}$). **b.** $\delta\Delta_+(\mathbf{r})$ map prepared using the same procedure outlined in Section C revealing the same gap modulations as Main Text Fig. 4a. **c.** The Fourier transform of $\delta\Delta_+(\mathbf{r})$ map, $\delta\Delta_+(\mathbf{q})$. ($\mathbf{P}_1, \mathbf{P}_2, \mathbf{P}_3$) PDW peaks are highlighted with dashed red circles and reciprocal lattice vectors highlighted with dashed orange circles.



Extended Data Fig. 9 Phase shift between CDW and PDW. (a,d,g) Inverse Fourier transforms of the three CDW wavevectors identified $g_{Q_i=1,2,3}(\mathbf{r}, -15 \text{ mV})$ in the same $10 \text{ nm} \times 10 \text{ nm}$ FOV as Main Text Fig. 3b. (b, e, h) Inverse Fourier transforms of the three PDW $\delta\Delta_{P_i=1,2,3}$ wavevectors in the same FOV as Main Text Fig. 3b. (c, f, i) Distributions of the relative spatial phase difference $\delta\phi_i(\mathbf{r})$ between $\phi_i^C(\mathbf{r})$ and $\phi_i^P(\mathbf{r})$ from three individual wavevectors. Each histogram is centered around π reinforcing the observation of a general phase difference $|\delta\phi_i| \cong \pi$ between the CDW and PDW.

METHODS REFERENCES:

1. Liu, X., Chong, Y. X. & Sharma, R. Discovery of a Cooper-pair density wave state in a transition-metal dichalcogenide. *Science* **1452**, 1447–1452 (2021).
2. Lawler, M. J. *et al.* Intra-unit-cell electronic nematicity of the high- T_c copper-oxide pseudogap states. *Nature* **466**, 347–351 (2010).